Article

Ligand Shell Thickness of PEGylated Gold Nanoparticles Controls Cellular Uptake and Radiation Enhancement

Paul T. Lawrence, Avery S. Daniels, Allison J. Tierney, E. Charles H. Sykes, and Charles R. Mace*

Read Online

ACCESS | Metrics & More | Article Recommendations | Supporting Information

ABSTRACT: The drive to improve the safety and efficacy of radiotherapies for cancers has prompted the development of nanomaterials that can locally amplify the radiation dose at a tumor without damaging the surrounding healthy tissue. Gold nanoparticles (Au NPs), in particular, exhibit promising radiosensitizing properties under kilovolt X-ray exposure, although the precise mechanism behind this enhancement is not fully understood. While most studies recognize the involvement of factors such as core composition, size, shape, and ligand chemistry in the effectiveness of Au NPs for radiation-induced cancer treatment, there is a scarcity of direct assessments that

connect the photophysical properties of the nanomaterial with the observed cellular or biological outcomes. Despite previous evidence of low-energy electron (LEE) emission from Au NPs and their potential to initiate biological damage, to our knowledge, no studies directly correlate the secondary LEE emission with radiation-induced cell death. In this study we assessed Au NPs functionalized with polyethylene glycol (PEG) ligands of varying molecular weights and lengths (1, 5, and 20 kDa PEG) as potential radiosensitizers of A549 lung cancer cells using kilovolt X-ray source potentials (33−130 kVp). We assessed NP internalization using mass cytometry, radiation dose enhancement using clonogenic survival assays, and secondary LEE emission using a retarding field analyzer. Results reveal a statistically significant difference in cellular uptake and radiation dose enhancement for 5 kDa PEG-Au NPs compared to formulations using 1 and 20 kDa PEG, while analysis of secondary LEE emission spectra demonstrated that differences in the length of the PEG ligand did not cause statistically significant attenuation of secondary LEE flux. Consequently, we inferred increased cellular uptake of NPs to be the cause for the observed enhancement in radiosensitivity for 5 kDa PEGylated Au NPs. The approach used in this study establishes a more complete workflow for designing and characterizing the performance of nanomaterial radiosensitizers, allowing for quantification of secondary LEEs and cellular uptake, and ultimately correlation with localized dose enhancement that leads to cell death.
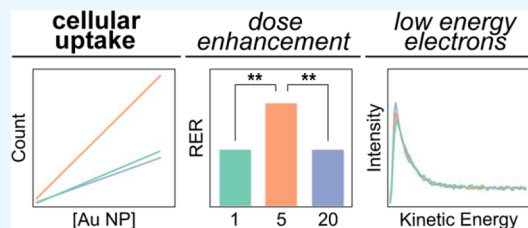
1. INTRODUCTION

The development of nanomaterials as radiation dose enhancers is a direct result of increasing interest in improving radiation therapy for patients. Gold nanoparticles (Au NPs) have promising performances as radiosensitizers both *in vitro* and *in vivo* when exposed to kilovolt X-rays even though the specific mechanism of action driving radiation enhancement is complex and has yet to be elucidated fully.[1−7] The photophysical properties of bulk materials, as well as their mass attenuation coefficients, provide some insight into localized effective dosing, but the downstream photochemical, biochemical, and biological effects that ultimately result in cell death remain poorly understood.[8−10] Investigations into these mechanisms produce varied results, which demonstrates the disparity between theoretical calculations of radiosensitization based on the mass attenuation coefficient of bulk gold and the observed experimental findings in culture or animal models.[11−13] Monte Carlo simulations of energy-dependent, high atomic weight materials help bridge the gap between theoretical predictions and experimental observations of kilovolt X-ray dose enhancement in biological systems; however, these simulations focus solely on physical effects

and are not fully representative, which leads to underestimation of damage. Additionally, these studies describe diverse nanomaterial types and sizes that are irradiated by a wide range of X-ray conditions (e.g., dose, energy, and source), provide unique energy spectra, and report various methods of assessing cell death, collectively posing challenges for the direct comparison of results across the literature. While most reports acknowledge that many factors play a role in the efficacy of Au NPs for radiation-induced cancer therapy, direct evaluations of the relationship between physical inputs and biological outputs are limited.

Gold nanoparticles have been shown to locally enhance the absorption of ionizing radiation.[14,15] Experimental evidence indicates that when radiation (e.g., X-rays or high energy
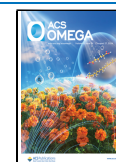
electrons) interacts with matter, including Au NPs, the vast majority of the primary excitation energy produces secondary LEEs between 0−10 eV, regardless of the source of primaries or their energy, with the maximum secondary LEE flux typically at ∼4−5 eV.[15−18] Due to their abundance and their ability to directly or indirectly cause genotoxic damage, these secondary LEEs are thought to be the primary driver of genotoxic damage in radiation-induced cancer therapy.[19−26] Many studies have investigated and quantified secondary LEE emission from NPs or planar samples.[18,27] Despite evidence of secondary LEE emission from NPs, and the efficacy of Au NPs for radiation-induced cancer therapy, relatively few investigations exist that correlate secondary LEE emission from NPs with radiation-induced damage to macromolecules or cells.[28−31] While these reports have provided valuable insight into the potential for Au NPs to serve as radiosensitizers, to our knowledge there are no reports where secondary LEE emission from NP samples is directly correlated to *in vitro* radiation dose enhancement. For example, one report demonstrates that when thiol-terminated ligands are bound to Au NPs, photoemission was enhanced; however, no claims were made relating this enhancement to increased death in cancer cells.[32]

While unfunctionalized Au NPs alone may act as irradiation enhancers,[33,34] NPs are typically functionalized with ligands to stabilize against aggregation or lower the potential for cytotoxicity. While some modifications are passive and done strictly to protect the Au NP core, other surface modifications may provide site-specific targeting on or in the cell (e.g., to surface markers or organelles) to increase and localize radiosensitivity.[35−39] One such study of Au NP modifications correlated surface ligand length with DNA damage and *in vacuo* secondary LEE emission, revealing a relationship between secondary LEE attenuation and ligand length, whereby longer ligands resulted in less DNA damage than shorter ligands.[29] It is currently unknown if these results correlate with the more complex matrices that comprise a cellular environment, which further reinforces the need for experiments that link physical and biological processes.

The variable space that must be studied to develop nanoparticle-based radiosensitizers is vast, inclusive of core material composition, size, shape, and the chemistry of surface coatings.[40,41] With so many possible NPs and modifications, one must rigorously correlate irradiation conditions (i.e., dose, dose rate, energy) with cell viability and death (i.e., the desired emergent property) to design an optimal formulation. Furthermore, it is valuable to study the relationship between ligand chemistry and radiation dose enhancement and establish methods to ensure that Au NP ligand chemistries do not impact their photophysical properties. To conduct such studies, we chose to evaluate the impact that polyethylene glycol (PEG) coatings have on the performance of Au NPs radiosensitizers. PEG is known to stabilize Au NPs against aggregation, has excellent biocompatibility, and allows for ligand shell thickness to be changed while conserving the chemical composition simply by varying the PEG chain length.[42−44] By altering (i) the X-ray energy, dose rate, and total dose, (ii) the thickness of the PEG ligand shell, and (iii) the concentration of PEG-Au NPs added to media, we can begin to evaluate the conditions that lead to the highest degrees of radiosensitization. The ability to quantify cellular uptake, long-term cell death post-irradiation dose, and secondary LEE emission can provide critical, and currently

lacking, insight into the biological, biochemical, and photophysical factors resulting in cell death.

Herein, we examined the performance of 1, 5, and 20 kDa PEG-Au NPs as radiosensitizers of a lung carcinoma epithelial cell line (A549) over a range of X-ray peak energies (kVp), doses (Gy), and dose rates (Gy/min) to determine the effect that ligand shell thickness has on radiosensitization. We used mass cytometry to quantify the internalization of the PEG-Au NP prior to X-ray exposure. We then determined the kilovolt X-ray dependent radiation dose enhancement based on the long-term survival of A549 cells through a standard clonogenic survival assay and observed a statistically significant radiation dose enhancement for a single Au NP formulation (5 kDa PEG Au NPs). Finally, we measured the secondary LEE emission from each formulation *in vacuo* utilizing a retarding field analyzer. Our results provide evidence that secondary LEEs are not attenuated by a PEG ligand shell, over a range of thickness from 5−45 nm, as we observed no statistically significant difference in secondary LEE emission between formulations. Given these results, we infer that the observed increased radiation dose enhancement is due to increased cellular uptake of NPs. Furthermore, our method provides a workflow for designing and characterizing nanoparticle radiosensitizers where secondary LEE generation and cellular uptake can be quantified and then correlated to localized dose enhancement leading to cell death.

2. EXPERIMENTAL METHODS

2.1. PEG-Au NP Internalization via Mass Cytometry.
Twenty hours after cell incubation with 0.08−4 μg mL^{-1} PEG-Au NPs, we aspirated culture media, and washed cultures thrice with sterile PBS. We treated cells with 0.25% trypsin/EDTA dissociation reagent for 5 min, then neutralized the trypsin/EDTA with an equal volume of complete F-12K media, and recovered cells from wells by serological pipet. We then stained all samples with Cell-ID cisplatin according to published manufacture protocol and fixed the samples according to Maxpar Cytoplasmic/Secreted Antigen Staining with Fresh Fix protocol. This approach agrees with several previously published reports that quantified intracellular inorganic nanomaterials.[45,46]

Briefly, we recovered all cells by pelleting at 200 × g for 5 min and then washed the cells with 2 mL of warm serum free F12−K media. We determined initial cell counts using Countess II Automated Cell Counter (Thermo Fisher Scientific) before performing a final wash and resuspending cells in an appropriate volume of serum free F-12K media to achieve a final count of 2.0 × 10^7 cells mL^{-1}. We next made a 6 μM stock solution of Cell-ID cisplatin in prewarmed (37 °C), serum free, F-12K media and added an equal volume of this staining solution to samples of cells to create final concentrations of 1.0 × 10^7 cell mL^{-1} in 3 μM cisplatin-containing complete media, with volumes ranging from 30−60 μL based on harvest cell count. We incubated samples for 5 min at 37 °C with 5% CO$_2$, and then we added 500 μL of complete F-12K media to each sample to sequester unbound cisplatin. We then pelleted and washed the cells with an additional 500 μL of complete F-12K media. After pelleting, we aspirated the supernatant, resuspended the cell pellets in residual volume of supernatant, and added 1 mL of 1.6% paraformaldehyde prepared in 1x Maxpar PBS. We gently vortexed the cells and incubated them at 22 °C for 10 min. After fixation, we pelleted the cells and stained them with 42

nM Cell-ID Intercalator-Ir, prepared in Maxpar Fix/Perm Buffer. Immediately prior to sample acquisition, we washed all cells once with 2 mL of Maxpar Cell Staining Buffer and twice with Cell Acquisition Solution Plus (CAS+) and submitted these samples as pellets for analysis on a Standard Biotools CyTOF XT mass cytometer at the Longwood Medical Area mass cytometry core facility.

2.2. Long-Term Proliferation by Percent Area Image Analysis of A549 Cells.

The variable morphology of A549 colonies after exposure to ionizing radiation made qualifying long-term survival by conventional colony scoring highly subjective. This challenge has been addressed previously by quantifying long-term growth through comparisons of the area of cellular growth relative to the total culture surface area.[47−49] This automated image analysis eliminates the subjectivity of manual colony counting. We split all RGB composite images of colonies into individual color channels. We analyzed the green channel image (i.e., the channel with the highest contrast ratio for the Crystal Violet stain) using an ImageJ ColonyArea plugin.[47] In the few instances when the automated thresholding overestimated colony area, we performed a manual thresholding to accommodate for low signal-to-noise ratio. Prior to implementing %Area analysis as a surrogate for counting individual colonies, we confirmed there was strong agreement between seeding density and resultant %Area (Figure S5).

2.3. Energy Dependent Dose Enhancement.

We incubated A549 cultures with 0.4 μg mL^{-1} 5 kDa PEG-Au NP 20 hours prior to irradiation with 5 Gy of 33, 45, 90, and 130 kVp X-rays. We also prepared control populations of cultures without nanoparticle treatment to account for native plating efficiency and plating efficiency of A549 cells after X-ray exposure. We held the dose rate for all irradiations at 0.1 Gy min^{-1} by modulating the current used to generate X-rays of different incident energy. Then, we subjected all cultures to clonogenic survival assay to determine which incident energy induces the highest degree of radiosensitization given otherwise constant culturing and irradiation conditions.

2.4. Ligand Shell Effect in keV X-ray DE.

We determined formulation-specific RER measurements, using X-rays generated by an electrode potential of 90 kVp, using a constant nanoparticle concentration of 0.8 μg mL^{-1}. We added all PEG-Au NP formulations to cultures as described above, and then exposed each culture to 4 Gy of 90 kVp X-rays at 0.1 Gy min^{-1}. We then harvested and plated A549 cells for long-term growth assessment. After 8 days of growth, we processed resulting colonies and determined the RER$_{4Gy}$ as described above.

2.5. Secondary LEE Emission Spectra.

We performed secondary LEE emission measurements in an ultrahigh vacuum (UHV) chamber with a base pressure $<1.0 \times 10^{-9}$ mbar. The UHV chamber comprises an OCI Vacuum Engineering low energy electron diffraction (LEED)/Auger electron spectroscopy (AES) system model LPS-D series, which contained a retarding field analyzer (RFA) model RFA-I-USB (Figure S6). We used a freshly cleaved, highly ordered pyrolytic graphite (HOPG) mounted on a Ta sample plate from Omicron NanoTechnology as the support for the NPs in the Auger characterization and secondary LEE emission measurements. We drop cast 20 μL of samples containing 2.0×10^{12} NPs of each formulation onto the HOPG substrate. Assuming spherical Au NPs and the drop cast spot being 0.25 cm in radius, we conservatively estimate a film thickness of ∼7 nm.

This film thickness is sufficiently thick to ensure that secondary LEE emission comes from the NP film and not the HOPG substrate. To acquire secondary LEE emission spectra, we excited the NP samples with a 200 eV electron beam while the RFA was used to measure electron emission as a function of retarding potential, which was then plotted as a secondary LEE emission spectrum (Figure S7). We applied a −50 V bias to each sample to increase the number of secondary LEEs reaching the analyzer. For each NP formulation, we recorded secondary LEE emission with an electron beam current of 0.5 μA, 1.0 μA, 2.0 μA, and 3.0 μA. At each beam current, we recorded five consecutive spectra to ensure reproducibility and then averaged the spectra. Furthermore, we measured three separate drop cast samples of each formulation to account for differences in NP sample drying. It is important to note that our measurements quantify the energy and flux of all emitted electrons including those that have undergone both elastic and inelastic scattering.

2.6. NP Characterization in Vacuum with Auger Electron Spectroscopy.

To characterize the NP formulations in vacuum and ensure that the recorded secondary LEE emission was from the NPs, we utilized AES. While secondary LEE emission measurements were excited with a 200 eV electron beam, during Auger characterization we excited the samples with a 2000 eV electron beam having a beam current of ∼70 μA, a focus of 1600 V, a Wehnelt of 30 V, and a modulation voltage of 5 V. We recorded secondary LEE emission spectra before performing AES measurements and the same area of the sample was studied in AES and secondary LEE emission experiments. Additionally, no evidence of beam damage was found as spectra were reproducible between separate Auger experiments.

3. RESULTS AND DISCUSSION

3.1. PEG-Au NP Characterization.

PEG-Au NPs are used commonly in NP formulations intended for cellular uptake.[50−53] We chose to use 5 nm Au NP as the core particle due evidence that this core size supports Au NP size-dependent X-ray dose enhancement.[54] We avoided highly polydisperse NP suspensions by conjugating thiol-terminated PEGs to the Au NP surface.[55] UV−vis measurements of PEG-Au NPs formulations retained the characteristic 520 nm surface plasmon resonance peak of the starting 5 nm citrate-capped Au NP after ligand conjugation (Figure S1A). The retention of this peak indicates that ligand conjugation did not induce aggregation. We used dynamic light scattering to show that the hydrodynamic diameter of all PEG-Au NPs increased as a function of PEG molecular weight from 1 kDa to 20 kDa (Figure 1A, Figure S1C) and that all formulations were monodisperse. While the hydrodynamic diameter increased as the PEG molecular weight increased, the zeta potentials became more neutral. (Table S1). This approach afforded us control for size-dependent X-ray dose enhancement associated with Au NPs with a common core composition to examine specifically the impact of ligand chemistry on radiation dose enhancement and generation of secondary LEE.

3.2. PEG-Au NP Internalization via Mass Cytometry.

Quantifying intracellular Au NP content at the time of X-ray exposure is a critical aspect of characterizing X-ray dose enhancement and comparing different particle formulations. Prior to mass cytometry analysis, we ensured there were no background cytotoxic effects via a metabolic (3-(4,5-dimethylthiazol-2-yl)-2,5-diphenyltetrazolium bromide) tetra-
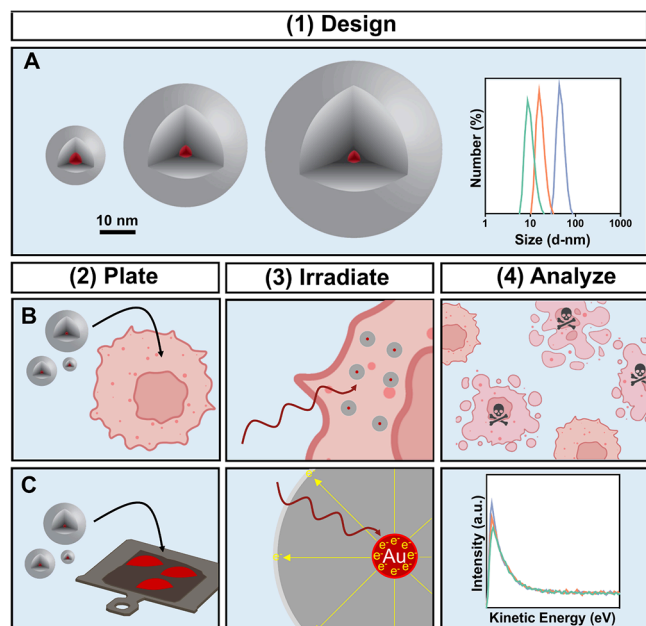
Figure 1. Experimental workflow. (A) We modified 5 nm citrate-capped Au NPs with 1, 5, or 20 kDa thiol-terminated PEG. The resulting particles were monodisperse and had hydrodynamic diameters proportional to molecular weight as shown in the right panel. (B) We determined dose enhancement from A549 lung cancer cells incubated with PEGylated Au NPs and irradiated with kilovolt X-rays. (C) We measured low energy electron emission from each particle type.
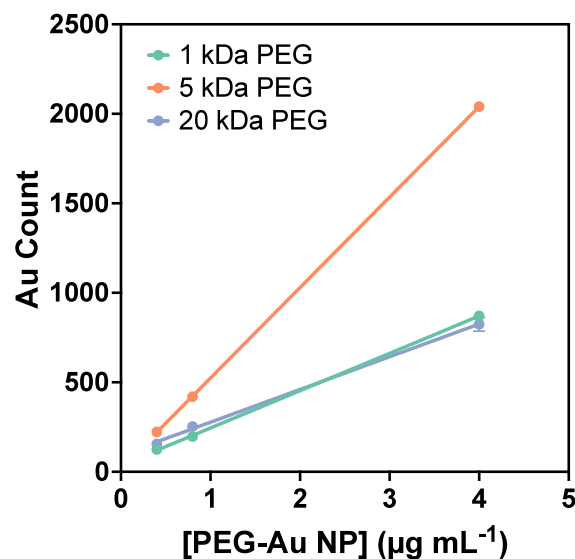

Figure 2. Internalization of PEG-Au NP by A549 cells as determined using mass cytometry. Cells were incubated with 1 kDa, 5 kDa, and 20 kDa PEG-Au NP at 0.4, 0.8, and 4.0 μg mL^{-1} for 20 h ($N = 3$). The reported Au Counts are the average Au mass counts greater than 5000 single cell events obtained during mass cytometry runs. Internalization is reported as mean mass spectroscopic count following data processing as described in Figure S3. The error bars indicate the standard deviation of Au mass counts for each cell population analyzed. All data was fit to linear regressions ($R^2 = 0.9977$, 0.9998, and 0.9873 for 1 kDa, 5 kDa, and 20 kDa PEG-Au NPs, respectively).

zolium (MTT) reduction assay (Figure S2). Our results show that cell populations retain >80% of their metabolic activity after exposure to all three PEG-Au NP formulations for concentrations up to 8 μg mL^{-1}. We used mass cytometry to measure the internalization of 1 kDa, 5 kDa, and 20 kDa PEG-Au NP. We chose low concentrations (ca. μg mL^{-1}) to align our experiments with a more drug-like regime even though other reports of radiation dose enhancement use much higher doses (mg mL^{-1}).[40,56,57] Under all experimental conditions, CellID-Cisplatin staining indicated that cell populations retained greater than 90% viability based on exclusion of cisplatin by intact cell membranes. We performed mass cytometry data cleanup, viability gating, and singlet gating prior to reporting mean intracellular Au content (Figure S3). We chose a range of 0.4, 0.8, and 4.0 μg mL^{-1} based on the agreement of the MTT and CellID-Cisplatin viability assays. We demonstrate a relationship between the concentration of PEG-Au NP in cell culture media and internalization over the tested concentration range (Figure 2). The 5 kDa PEG-Au NP internalized better than either the 1 kDa PEG-Au NP or 20 kDa PEG-Au NP at all concentrations tested (Table S2). Preferential internalization of the intermediate PEG-Au NP size is likely due to optimal ligand protein corona formation.[58] This preferential uptake motivated us to use the 5 kDa PEG-Au NP formulation to examine variables related to energy dependent dose enhancement.

3.3. Defining and Quantifying Radiation Dose Enhancement.
Clonogenic survival assays are the most widely used technique to monitor colony formation of irradiated cells. This *in vitro* technique assesses radiation cytotoxicity by evaluating the ability of a cell to proliferate post-irradiation and form a colony. Cells unable to form a

colony have lost reproductive abilities and are considered nonviable. To assess and quantify post-irradiation viability, we first assigned a plating efficiency (PE) to each sample (eq 1). In most cases, cells form irregular colony shapes, so we calibrated PE based on the percent total area of the plate occupied by cells and not absolute counts as previously demonstrated.[59] We then calculated survival fractions (SF), which relate the PE of an irradiated sample (e.g., at 5 Gy) to the PE of a nonirradiated (i.e., at 0 Gy) sample (eq 2). Reports of radiation dose enhancement lack a common scale to quantify radiation effects.[60] In some cases, "iso-effect" values are reported, where different doses of radiation are compared using a dose modifying ratio, whereas others report "iso-dose" values, where different effects are monitored at a single dose. We chose an iso-dose approach to quantify different degrees of *in vitro* radio enhancement. We quantified the radiosensitization of cells using different formulations of Au NPs at a given radiation dose using the radiation dose enhancement ratio (RER), which normalizes the survival fraction of culture growth to the SF of cultures not irradiated but still in the presence of NPs for a specific dose (eq 3).[60]

$$ PE = \frac{Area(\%)}{Seeding\ Density} \tag{1} $$

$$ SF_{XGy} = \frac{PE_{XGy}}{PE_{0Gy}} \tag{2} $$

$$ RER_{XGy} = \frac{SF_{0Gy}}{SF_{XGy}} \tag{3} $$

The RER value encompasses multiple variables of interest, including plating efficiency, radiation dose enhancement, and

cyto- and radiotoxicity. These values can also be stated as a percent, relative to non-irradiated samples, allowing for comparison across literature. Experimentally calculated RER values typically afford a higher enhancement than those calculated using Monte Carlo simulations, as this value also reflects any additional biological dose enhancement due to the cellular response to radiation.[9] We report all radiation dose enhancement values as RER, affording a more comprehensive understanding of iso-dose radiosensitization effects due to PEG-Au NPs.

3.4. Irradiation of PEG-Au NPs in Human Lung Carcinoma Cell Line.
The X-ray dose rate is a critical parameter in Au NP radiation enhancement, with higher dose rates inducing greater RER;[41] however, when determining energy dependent radiosensitization, it is critical to control for dose rate-dependent enhancement. We chose to modulate the filament current used to generate X-rays to dose cultures at a rate of 0.1 Gy min^{-1} for all incident X-ray energies. We determined RER due to 5 kDa PEG-Au NP based on the % Area of long-term culture growth (Figure S4) relative to initial seeding densities, which normalizes the survival fraction of culture growth relative to survival fractions of cultures not irradiated in the presence of 5 kDa PEG-Au NPs (Figure S5). Given a constant X-ray dose, dose rate, and concentration of 5 kDa PEG-Au NP (0.4 μg mL^{-1}), we found that 90 kVp X-rays induced 44% RER (Figure 3), which is much higher than would be expected relative to reports of RER at comparable dose rates.[41,61] Very modest degrees of RER were observed for 45 and 130 kVp X-rays (i.e., < 10%), with insignificant RER observed for 33 kVp X-rays.
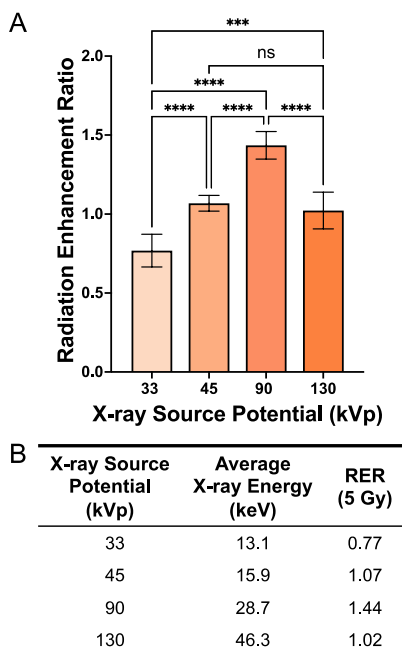

Figure 3. Radiation enhancement ratios (RER) for A549 cells as a function of X-ray source potential. Cells were irradiated at a single dose (5 Gy) and treated with a single formulation of PEG-Au NP (0.4 μg mL^{-1} of 5 kDa PEG-Au NP) to investigate the role of X-ray source potential on RER. (A) RER values at each potential compared by one-way ANOVA: *** (p < 0.001), **** (p < 0.0001). Error bars represent n = 6 replicates. (B) Table of applied X-ray source potentials (kVp) and calculated effective incident X-ray energy (keV) according the *SpekCalc* relative to RER values.

X-ray Source Potential (kVp)	Average X-ray Energy (keV)	RER (5 Gy)
33	13.1	0.77
45	15.9	1.07
90	28.7	1.44
130	46.3	1.02

After identifying optimal irradiation conditions for kVp X-ray radiation enhancement, we applied them to examine RER induced by three PEG-Au NP with incrementally thicker ligand shells. We found that sub μg mL^{-1} treatments of 1 kDa, 5 kDa and 20 kDa PEG-Au NPs all induced some degree of 90 kVp X-ray RER (Figure 4). Predictably, 5 kDa PEG-Au NPs
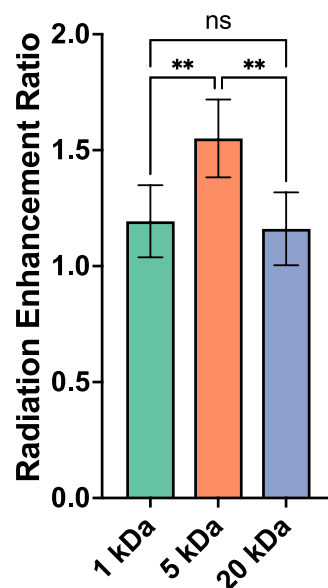

Figure 4. Radiation enhancement ratios (RER) as a function of single irradiation condition (4 Gy, 90 kVp X-rays) and nanoparticle concentration (0.8 μg mL^{-1}) to investigate the role of PEG molecular weight on functionalized Au NPs. A one-way ANOVA was performed for each RER value: ** (p < 0.01). Error bars represent n = 6 replicates.

induced a higher RER when incubated with cells at a higher concentration: 55% at 0.8 μg mL^{-1} versus 44% at 0.4 μg mL^{-1}. As a result of these experiments, given equal X-ray and NP exposure conditions, we demonstrated that the ligand formulation can significantly impact RER. We found that despite substantial internalization, 1 kDa and 20 kDa Au NPs only induced 19% and 16% dose enhancement, respectively. However, these differences may not be due to variable photophysical radiation enhancement. The preferential internalization of 5 kDa PEG-Au NP is the most likely reason for its higher relative RER to 1 kDa and 20 kDa PEG-Au NPs. To further explain these data, we investigated the NP formulations *in vacuo* to quantify secondary LEE emission from each sample.

3.5. Nanoparticle Characterization in Ultra-High Vacuum.
We hypothesized that the observed increase in RER for 5 kDa PEG-Au NPs compared to 1 kDa and 20k Da PEG-Au NPs was due to a combination of secondary LEE emission and NP cellular uptake. To determine the elemental composition of the surface and characterize the NPs in ultra-high vacuum (UHV), we performed Auger electron spectroscopy (AES) (Figure 5A) in which Auger transitions of elements in the sample were excited with 2000 eV electrons their intensities correlated with the amount of each element present. We found that the various NP formulations can be distinguished from one another based upon the intensity of the Au Auger peak. Specifically, the 1 kDa PEG-Au NPs had the highest intensity of Au Auger signal (demonstrated by an Auger peak at 69 eV), followed by 5 kDa PEG-Au NPs, while 20 kDa PEG-Au NPs showed no Auger signal for Au.
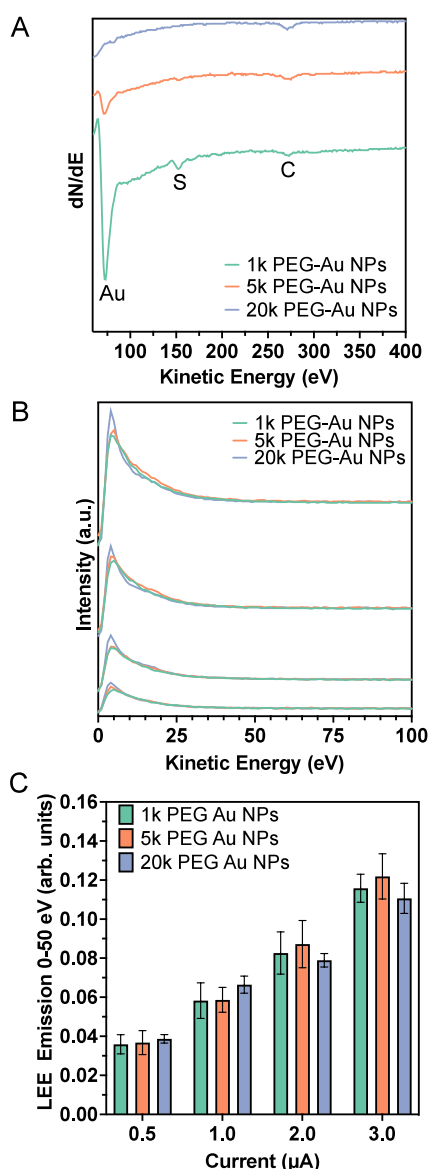
Figure 5. *In vacuo* secondary LEE emission and NP characterization. (A) Auger electron spectroscopy data for the various NP formulations. An electron beam energy of 2000 eV was used to excite the sample. The Auger peak at 69 eV is attributed to Au, 152 eV S, and 272 eV C. (B) Qualitative secondary LEE emission at beam currents of 0.5, 1.0, 2.0, and 3.0 μA (bottom to top, respectively). A bias of −50 V was applied to the sample and a 200 eV beam energy was used to excite the sample. (C) Quantitative secondary LEE emission in the 0−50 eV kinetic energy range (acquired by integrating from 0−50 eV) at various beam currents. Error bars are the standard deviation of the average emission for the three different drop cast samples.

Qualitatively, these data are consistent with the ligand lengths since the inelastic mean free path (IMFP) is ~0.5 nm for a 69 eV electron and the longer ligands attenuate the Auger signal from the Au core.[62] Furthermore, as the molecular weight of the PEG ligands increased, the Auger peak signal for carbon (C) at 272 eV increased, which is consistent with the increase in number of carbon atoms in the PEG chain as molecular weight increases from 1 kDa to 20 kDa. The Auger peak at 152 eV is attributed to sulfur (S), which was observed for 1 kDa and 5 kDa PEG-Au NPs, consistent with the PEG ligands

being thiolate terminated. However, the S Auger peak was not found for the 20 kDa PEG-Au NPs which can also be attributed to the longer ligand attenuating the S Auger peak signal from the thiolate-Au interface.

More quantitative evidence that the NP formulations are distinguishable in Auger spectra can be found in Table 1.

Table 1. Auger Peak Intensities and Ratios, Secondary LEE Emission Relative to Au(111), and RER Values for Au NP Formulations

Sample	Au AES to Au (111) Ratio	Carbon AES Peak Intensity ($\times 10^{-3}$)	Ratio of LEE Emission to Au (111) ± SEM[a]	RER (4 Gy) ± SD[b]
Au(111)	1.00	0.0	1.00 ± 0.00	
1 kDa	0.39	2.6	0.73 ± 0.03	1.19 ± 0.15
5 kDa	0.13	4.1	0.75 ± 0.03	1.55 ± 0.17
20 kDa	0.00	5.4	0.75 ± 0.03	1.16 ± 0.16

[a]n = 4 replicates. [b]n = 6 replicates.

There, we took the ratio of the Au Auger peak intensity for each sample to the Au Auger peak signal for a Au(111) single crystal, and also compared the C Auger peak intensity between samples. We expect that as the ligand shell increases, so would the attenuation of the Au Auger signal and the C Auger peak would increase. The data reflect this hypothesis as 1 kDa PEG had the highest NP sample Au to Au(111) Auger peak ratio and the lowest C Auger peak intensity, while 20 kDa PEG had the lowest Au to Au(111) Auger peak ratio and highest C Auger peak intensity.

3.6. Low Energy Electron Emission. As previously mentioned, when high energy radiation interacts with matter, secondary LEEs are the predominant species generated and are thought to be the primary driver of genotoxic damage in radiation induced cancer therapy. Therefore, we anticipated that measuring the secondary LEE emission from the Au NPs could shed light on the observed increase in RER demonstrated by the 5k PEG-Au NPs in comparison to the other formulations. We hypothesized that as the length of the ligand increased (1 kDa < 5 kDa < 20 kDa), the longer PEG ligands would lead to more attenuation of secondary LEEs. Surprisingly, however, this was not the case upon measuring the secondary LEE emission from the various PEG-Au NP formulations. Qualitatively, there was no obvious difference between secondary LEE emissions from the NP samples at the four different beam currents (Figure 5B). Also, as observed in previous studies, most of the electron emission is within the kinetic energy range of 0−10 eV, and therefore are low-energy secondry electrons and not, for instance, low energy Auger electrons. Additionally, our electron emission is peaked at ~4 eV where electrons have an IMFP of ~20 nm, and is also consistent with previous reports.[62] Integrating the areas under the curves from 0−50 eV for each secondary LEE spectrum facilitates quantitative comparisons of the total electron emission in this kinetic energy range between NP samples (Figure 5C). After the secondary LEE measurements, we verified that the secondary LEE emission originated from the NPs and not the graphite substrate by the aforementioned AES of the Au Auger signal which is only observed when NPs are present. One-way ANOVA tests indicate there is no statistically significant difference in secondary LEE emission from any of the different NP samples tested with beam currents 0.5−3.0 μA ($p > 0.34$ for all samples, $\alpha = 0.05$). To further strengthen

this interpretation, we normalized secondary LEE emission from PEGylated Au NPs to secondary LEE emission from a Au(111) single crystal (Table 1). The calculated ratio of LEE emission is the average ratio of sample secondary LEE emission to Au(111) secondary LEE emission at each beam current. These data also suggested there was no statistically significant difference ($p = 0.86$, $\alpha = 0.05$) between formulations, which supports previously reported MC simulations that concluded that various ligand compositions attached to Au NPs should not affect the flux of secondary LEEs.[63]

When comparing the secondary LEE emission with the RER values, it would be expected that if the emission from the various NP formulations was the same, then the RER would also be the same, assuming the different formulations have the same uptake. Instead, we found that 5k PEG-Au NPs had the highest RER at 55% and 1 kDa and 20 kDa PEG-Au NPs had similar RERs at 19% and 16%, respectively. This increase in the RER for 5 kDa PEG-Au NPs can be attributed to the greater internalization of the 5 kDa PEG-Au NPs than either the 1 kDa or 20 kDa PEG-Au NPs. Comparing results from 1 kDa and 20 kDa PEG-Au NPs further support these claims: their secondary LEE emission and cellular uptake are equal, as are their experimental RER values. Furthermore, while secondary LEEs are capable of inducing both direct and indirect genotoxic damage, our method is unable to distinguish between the two. The effective attenuation length (EAL), which is the distance at which the flux of electrons preserving their initial kinetic energy diminishes by 1/e, of 4 eV electrons in water is ∼3 nm.[64] Therefore, secondary LEEs must be generated within nm of DNA to directly induce genotoxic damage. However, secondary LEEs can indirectly cause genotoxic damage, for example via generation of reactive oxygen species (ROS), which effectively increases the distance over which LEEs can have an effect. Our combined approach of in vitro RER measurements and in vacuo secondary LEE measurements enables us to correlate the two, demonstrate that the secondary LEE emission from the three different PEG-Au NPs yield is similar, and conclude that differences in cellular uptake explain radiobiological effects.

4. CONCLUSIONS

In this manuscript, we evaluated the performance of PEGylated Au NPs as radiosensitizers of a lung carcinoma epithelial cell line (A549) by varying the thickness of the particle ligand shell using PEGs with different molecular weights (1, 5, and 20 kDa) and irradiating cultures using a range of X-ray peak energies (kVp), doses (Gy), and dose rates (Gy/min). We observed that there existed an optimum set of conditions—in peak X-ray source potential (90 kVp) and molecular weight of PEG (5 kDa) used to functionalize the Au NPs—that lead to a statistically significance dose enhancement, which we determined based on the long-term survival of irradiated cells using a clonogenic survival assay. We initially expected to see a trend in diminishing dose enhancement as a function of increasing the length of the PEG chains bound to the Au NP core: as the ligand shell thickness increased, the secondary LEE emission would decrease as emission from the Au core would be hindered.[29] However, our results provide evidence that secondary LEEs are not attenuated by a PEG ligand shell, at least over a range of thickness from 5−45 nm, as we observed no statistically significant difference in secondary LEE emission between particle formulations. Previous experiments by Xie et.

al have shown that when thiol terminated ligands are functionalized to Au NPs, as in the chemistry we used here, secondary LEEs generated from the Au core can be transmitted to and ejected through the thiol terminated ligands.[32] Additionally, previous Monte Carlo simulations have shown that various ligand coatings do not affect secondary LEE emission from the Au core.[63] Taken together, these two observations potentially explain why we observed equal secondary LEE emission for 1 kDa, 5 kDa, and 20 kDa PEG-Au NPs.

Instead of chemistry-induced photophysics as an explanation for differences in radiosensitization for particles under common irradiation conditions, measurements by mass cytometry suggest that particle uptake is the driving force for radiation enhancement in this system: particles functionalized with 5 kDa PEG were internalized approximately 2-fold more than those with 1 or 20 kDa PEGs, which resulted in 1.44-fold (44%) more enhancement of cell death for particles introduced to cultures at a final concentration of 0.8 μg mL^{-1}. Previous accounts of keV dose enhancement based on clonogenic survival of A549 cells have reported dose enhancement factor as high as 2.9-fold (190%);[65] however, this result was achieved at 500 times higher Au NP dosing, which supports in vitro research but is unlikely to translate to clinical applications. Investigation into the biocompatibility of Au NP have shown that even relatively low doses of Au NP (i.e., ≤10 μg mL^{-1} in vitro and 10 mg kg^{-1} in vivo) can significantly impact cellular growth, intracellular ROS, and expression of critical pro-apoptotic genes in the absence of radiation.[57,66] While evaluating additional cell lines and particle types would expand on and validate these observations, our combined results, and the workflow used to generate them, suggest a method for designing and characterizing nanomaterial-based radiosensitizers, whereby the system photophysics (e.g., secondary LEE generation, peak X-ray source voltage) and pharmacokinetics (i.e., dose-dependent cellular uptake) can be used to predict an emergent property: radiation enhancement. In fact, a recent review called for the need to investigate secondary LEE radiation damage in more realistic models.[35] Our approach enables the LEE spectrum of biocompatible Au nanopartilcles to be quantifed, compared between NP formulations and then related to the RER of three different PEG-Au NP formulations. This approach indicated that in this system, differences in cellular uptake was the drivng force behind different RER values. Translating nanomaterials into clinical practice requires substantial effort beyond what is required for in vitro testing, and, ultimately, we expect the ability to use this workflow to screen potential candidates will accelerate the research efforts needed to navigate this expansive space of particle types and formulations.

■ ASSOCIATED CONTENT

Ⓢ Supporting Information

The Supporting Information is available free of charge at https://pubs.acs.org/doi/10.1021/acsomega.4c06568.

> Materials and additional experimental methods: characterization of PEG-Au NPs, cell culture and dosing conditions, metabolic effects of PEG-Au NPs on A549 cells, clonogenic survival assays, mass cytometry gating scheme, correlation of plate percent area and seeding density of A549 cells, simulation of X-ray irradiation conditions, NP characterization in vacuo, schematic of

retarding field analyzer for low energy electron emission measurements, converting raw secondary LEEs to secondary LEE emission spectra (PDF)

AUTHOR INFORMATION

Corresponding Author

Charles R. Mace − *Department of Chemistry, Tufts University, Medford, Massachusetts 02155, United States;* ● orcid.org/0000-0003-3410-5014; Email: charles.mace@tufts.edu

Authors

Paul T. Lawrence − *Department of Chemistry, Tufts University, Medford, Massachusetts 02155, United States*

Avery S. Daniels − *Department of Chemistry, Tufts University, Medford, Massachusetts 02155, United States*

Allison J. Tierney − *Department of Chemistry, Tufts University, Medford, Massachusetts 02155, United States*

E. Charles H. Sykes − *Department of Chemistry, Tufts University, Medford, Massachusetts 02155, United States;* ● orcid.org/0000-0002-0224-2084

Complete contact information is available at:
https://pubs.acs.org/10.1021/acsomega.4c06568

Notes

The authors declare no competing financial interest.

REFERENCES

(1) Penninckx, S.; Heuskin, A. C.; Michiels, C.; Lucas, S. The role of thioredoxin reductase in gold nanoparticle radiosensitization effects. *Nanomedicine* **2018**, *13*, 2917−2937.

(2) Bromma, K.; Cicon, L.; Beckham, W.; Chithrani, D. B. Gold nanoparticle mediated radiation response among key cell components of the tumour microenvironment for the advancement of cancer nanotechnology. *Sci. Rep.* **2020**, *10*, No. 12096.

(3) Hainfeld, J. F.; Slatkin, D. N.; Smilowitz, H. M. The use of gold nanoparticles to enhance radiotherapy in mice. *Phys. Med. Biol.* **2004**, *49*, N309−N315.

(4) Seltzer, S. M. Calculations of Photon Mass Energy-Transfer and Mass-Absorption Coefficients. *Radiat. Res.* **1993**, *136*, 147−170.

(5) Ghita, M.; McMahon, S.; Taggart, L.; Butterworth, K. T.; Schettino, G.; Prise, K. M. A mechanistic study of gold nanoparticle radiosensitisation using targeted microbeam irradiation. *Sci. Rep.* **2017**, *7*, No. 44752.

(6) Butterworth, K. T.; McMahon, S. J.; Taggart, L. E.; Prise, K. M. Radiosensitization by gold nanoparticles: effective at megavoltage energies and potential role of oxidative stress. *Transl. Cancer Res.* **2013**, *2*, 269−279.

(7) Rahman, W. N.; Geso, M.; Yagi, N.; Abdul Aziz, S. A.; Corde, S.; Annabell, N. Optimal energy for cell radiosensitivity enhancement by gold nanoparticles using synchotron-based monoenergetic photon beams. *Int. J. Nanomed.* **2014**, *9*, 2459−2467.

(8) Butterworth, K. T.; McMahon, S. J.; Currell, F. J.; Prise, K. M. Physical basis and biological mechanisms of gold nanoparticle radiosensitization. *Nanoscale* **2012**, *4*, 4830−4838.

(9) Kempson, I. Mechanisms of nanoparticle radiosensitization. *Wiley Interdiscip. Rev. Nanomed. Nanobiotechnol.* **2021**, *13*, No. e1656.

(10) Srinivasan, K.; Samuel, E. J. J. Target biological tissue and energy influence on dose enhancement factor produced by gold nanoparticles and its relevant radiological properties. *Radiat. Phys. Chem.* **2020**, *174*, No. 108912.

(11) Lin, Y.; McMahon, S. J.; Scarpelli, M.; Paganetti, H.; Schuemann, J. Comparing gold nano-particle enhanced radiotherapy with protons, megavoltage photons and kilovoltage photons: a Monte Carlo simulation. *Phys. Med. Biol.* **2014**, *59*, 7675.

(12) Poignant, F.; Charfi, H.; Chan, C.-H.; Dumont, E.; Loffreda, D.; Gervais, B.; Beuve, M. Monte Carlo simulation of free radical production under keV photon irradiation of gold nanoparticle aqueous solution. Part II: Local primary chemical boost. *Radiat. Phys. Chem.* **2021**, *179*, No. 109161.

(13) Sotiropoulos, M.; Henthorn, N. T.; Warmenhoven, J. W.; Mackay, R. I.; Kirkby, K. J.; Merchant, M. J. Modelling direct DNA damage for gold nanoparticle enhanced proton therapy. *Nanoscale* **2017**, *9*, 18413−18422.

(14) Arumainayagam, C. R.; Lee, H.-L.; Nelson, R. B.; Haines, D. R.; Gunawardane, R. P. Low-energy electron-induced reactions in condensed matter. *Surf. Sci. Rep.* **2010**, *65*, 1−44.

(15) Pimblott, S. M.; LaVerne, J. A. Production of low-energy electrons by ionizing radiation. *Radiat. Phys. Chem.* **2007**, *76*, 1244−1249.

(16) Pronschinske, A.; Pedevilla, P.; Murphy, C. J.; Lewis, E. A.; Lucci, F. R.; Brown, G.; Pappas, G.; Michaelides, A.; Sykes, E. C. Enhancement of low-energy electron emission in 2D radioactive films. *Nat. Mater.* **2015**, *14*, 904−907.

(17) Zhou, L.-H.; Cao, S.-Y.; Sun, T.; Wang, Y.-L.; Ma, J. A refined Monte Carlo code for low-energy electron emission from gold material irradiated with sub-keV electrons. *Nucl. Sci. Technol.* **2023**, *34*, 54.

(18) Casta, R.; Champeaux, J.-P.; Sence, M.; Moretto-Capelle, P.; Cafarelli, P. Comparison between gold nanoparticle and gold plane electron emissions: a way to identify secondary electron emission. *Phys. Med. Biol.* **2015**, *60*, 9095−9105.

(19) Baccarelli, I.; Bald, I.; Gianturco, F. A.; Illenberger, E.; Kopyra, J. Electron-induced damage of DNA and its components: Experiments and theoretical models. *Phys. Rep.* **2011**, *508*, 1−44.

(20) Zheng, Y.; Sanche, L. Mechanisms of Nanoscale Radiation Enhancement by Metal Nanoparticles: Role of Low Energy Electrons. *Int. J. Mol. Sci.* **2023**, *24*, 4697.

(21) Simons, J. How do low-energy (0.1−2 eV) electrons cause DNA-strand breaks? *Acc. Chem. Res.* **2006**, *39*, 772−779.

(22) Alizadeh, E.; Orlando, T. M.; Sanche, L. Biomolecular damage induced by ionizing radiation: the direct and indirect effects of low-energy electrons on DNA. *Annu. Rev. Phys. Chem.* **2015**, *66*, 379−98.

(23) Orlando, T. M.; Oh, D.; Chen, Y.; Aleksandrov, A. Low-energy electron diffraction and induced damage in hydrated DNA. *J. Chem. Phys.* **2008**, *128*, No. 195102.

(24) Siefermann, K. R.; Liu, Y.; Lugovoy, E.; Link, O.; Faubel, M.; Buck, U.; Winter, B.; Abel, B. Binding energies, lifetimes and implications of bulk and interface solvated electrons in water. *Nat. Chem.* **2010**, *2*, 274−279.

(25) Boudaïffa, B.; Cloutier, P.; Hunting, D.; Huels, M. A.; Sanche, L. Resonant formation of DNA strand breaks by low-energy (3 to 20 eV) electrons. *Science* **2000**, *287*, 1658−1660.

(26) Zheng, Y.; Sanche, L. Gold nanoparticles enhance DNA damage induced by anti-cancer drugs and radiation. *Radiat. Res.* **2009**, *172*, 114−119.

(27) Walker, C. G. H.; El-Gomati, M. M.; Assa'd, A. M. D.; Zadrazil, M. The secondary electron emission yield for 24 solid elements excited by primary electrons in the range 250−5000 ev: a theory/experiment comparison. *Scanning* **2008**, *30*, 365−380.

(28) Schlatholter; Lacombe, S.; Eustache, P.; Porcel, E.; Salado, D.; Stefancikova, L.; Tillement, O.; Lux, F.; Mowat, P.; van Goethem, M.-J.; et al. Improving proton therapy by metal-containing nanoparticles: nanoscale insights. *Int. J. Nanomed.* **2016**, *11*, 1549−1556.

(29) Xiao, F.; Zheng, Y.; Cloutier, P.; He, Y.; Hunting, D.; Sanche, L. On the role of low-energy electrons in the radiosensitization of DNA by gold nanoparticles. *Nanotechnology* **2011**, *22*, No. 465101.

(30) Gao, Y.; Zheng, Y.; Sanche, L. Low-Energy Electron Damage to Condensed-Phase DNA and Its Constituents. *Int. J. Mol. Sci.* **2021**, *22*, 7879.

(31) Huwaidi, A.; Kumari, B.; Robert, G.; Guérin, B.; Sanche, L.; Wagner, J. R. Profiling DNA damge induced by irradiation of DNA with gold nanoparticles. *J. Phys. Chem. Lett.* **2021**, *12*, 9947−9954.

(32) Xie, X. N.; Gao, X.; Qi, D.; Xie, Y.; Shen, L.; Yang, S.-W.; Sow, C. H.; Wee, A. T. S. Chemically linked AuNP-alkane network for enhanced photoemission and field emission. *ACS Nano* **2009**, *3*, 2722−2730.

(33) Hainfeld, J. F.; Slatkin, D. N.; Smilowitz, H. M. The use of gold nanoparticles to enhance radiotherapy in mice. *Phys. Med. Biol.* **2004**, *49*, N309−N315.

(34) Chithrani, D. B.; Jelveh, S.; Jalali, F.; van Prooijen, M.; Allen, C.; Bristow, R. G.; Hill, R. P.; Jaffray, D. A. Gold Nanoparticles as Radiation Sensitizers in Cancer Therapy. *Radiat. Res.* **2010**, *173*, 719−728.

(35) Narayanan S J, J.; Tripathi, D.; Verma, P.; Adhikary, A.; Dutta, A. K. Secondary electron attachement-induced radiation damage to genetic materials. *ACS Omega* **2023**, *8*, 10669−10689.

(36) Chithrani, D. B.; Dunne, M.; Stewart, J.; Allen, C.; Jaffray, D. A. Cellular uptake and transport of gold nanoparticles incorporated in a liposomal carrier. *Nanomedicine* **2010**, *6*, 161−169.

(37) Özçelik, S.; Pratx, G. Nuclear-targeted gold nanoparticles enhance cancer cell radiosensization. *Nanotechnology* **2020**, *31*, No. 415102.

(38) Oladimeji, O.; Akinyelu, J.; Daniels, A.; Singh, M. Modified Gold Nanoparticles for Efficient Delivery of Betulinic Acid to Cancer Cell Mitochondria. *Int. J. Mol. Sci.* **2021**, *22*, 5072.

(39) Stefanick, J. F.; Ashley, J. D.; Kiziltepe, T.; Bilgicer, B. A Systematic Analysis of Peptide Linker Length and Liposomal Polyethylene Glycol Coating on Cellular Uptake of Peptide-Targeted Liposomes. *ACS Nano* **2013**, *7*, 2935−2947.

(40) Ma, N.; Wu, F.-G.; Zhang, X.; Jiang, Y.-E.; Jia, H.-R.; Wang, H.-Y.; Li, Y.-H.; Liu, P.; Gu, N.; Chen, Z. Shape-Dependent Radiosensitization of Gold Nanostructures in Cancer Radiotherapy: Comparison of Gold Nanoparticles, Nanostars, and Nanorods. *ACS Appl. Mater. Interfaces* **2017**, *9*, 13037−13048.

(41) Morozov, K. V.; Kolyvanova, M. A.; Kartseva, M. E.; Shishmakova, E. M.; Dement'eva, O. V.; Isagulieva, A. K.; Salpagarov, M. H.; Belousov, A. V.; Rudoy, V. M.; Shtil, A. A.; Samoylov, A. S.; Morozov, V. N. Radiosensiitization by Gold Nanoparticles: Impact of the Size, Dose Rate, and Photon Energy. *Nanomaterials* **2020**, *10*, 952−968.

(42) Spaas, C.; Dok, R.; Deschaume, O.; De Roo, B.; Vervaele, M.; Seo, J. W.; Bartic, C.; Hoet, P.; Van den Heuvel, F.; Nuyts, S.; Locquet, J.-P. Dependence of Gold Nanoparticle Radiosensitization on Functionalizing Layer Thickness. *Radiat. Res.* **2016**, *185*, 384−392.

(43) Zhang, X.-D.; Wu, D.; Shen, X.; Chen, J.; Sun, Y.-M.; Liu, P.-X.; Liang, X.-J. Size-dependent radiosensitization of PEG-coated gold nanoparticles for cancer radiotherapy. *Biomaterials* **2012**, *33*, 6408−6419.

(44) Colangelo, E.; Comenge, J.; Paramelle, D.; Volk, M.; Chen, Q.; Lévy, R. Characterizing self-assembled monolayers on gold nanoparticles. *Bioconjugate Chem.* **2017**, *28*, 11−22.

(45) Nisa, L.; Francica, P.; Giger, R.; Medo, M.; Elicin, O.; Friese-Hamim, M.; Wilm, C.; Stroh, C.; Bojaxhiu, B.; Quintin, A.; et al. Targeting the MET Receptor Tyrosine Kinase as a Strategy for Radiosensitization in Locoregionally Advanced Head and Neck Squamous Cell Carcinoma. *Mol. Cancer Ther.* **2020**, *19*, 614−626.

(46) Li, S.; Ju, Y.; Zhou, J.; Noi, K. F.; Mitchell, A. J.; Zheng, T.; Kent, S. J.; Porter, C. J. H.; Caruso, F. Quantitatively Tracking Bio−Nano Interactions of Metal−Phenolic Nanocapsules by Mass Cytometry. *ACS Appl. Mater. Interfaces* **2021**, *13*, 35494−35505.

(47) Guzmán, C.; Bagga, M.; Kaur, A.; Westermarck, J.; Abankwa, D. ColonyArea: an ImageJ plugin to automatically quantify colony formation in clonogenic assays. *PLoS One* **2014**, *9*, No. e92444.

(48) Brix, N.; Samaga, D.; Hennel, R.; Gehr, K.; Zitzelsberger, H.; Lauber, K. The clonogenic assay: robustness of plating efficiency-based analysis is strongly compromised by cellular cooperation. *Radiat. Oncol.* **2020**, *15*, 248.

(49) Franken, N.; Rodermond, H.; Stap, J.; Haveman, J.; van Bree, C. Clonogenic assay of cells in vitro. *Nat. Protoc.* **2006**, *1*, 2315−2319.

(50) Coughlin, B. P.; Lawrence, P. T.; Lui, I.; Luby, C. J.; Spencer, D. J.; Sykes, E. C. H.; Mace, C. R. Evidence for biological effects in the radiosensitization of leukemia cell lines by PEGylated gold nanoparticles. *J. Nanopart. Res.* **2020**, *22*, 53.

(51) Matczuk, M.; Ruzik, L.; Aleksenko, S. S.; Keppler, B. K.; Jarosz, M.; Timerbaev, A. R. Analytical methodology for studying cellular uptake, processing and localization of gold nanoparticles. *Anal. Chim. Acta* **2019**, *1052*, 1−9.

(52) Kalimuthu, K.; Lubin, B. C.; Bazylevich, A.; Gellerman, G.; Shpilberg, O.; Luboshits, G.; Firer, M. A. Gold nanoparticles stabilize peptide-drug-conjugates for sustained targeted drug delivery to cancer cells. *J. Nanobiotechnol.* **2018**, *16*, 34.

(53) Dubaj, T.; Kozics, K.; Sramkova, M.; Manova, A.; Bastús, N. G.; Moriones, O. H.; Kohl, Y.; Dusinska, M.; Runden-Pran, E.; Puntes, V.; Nelson, A.; Gabelova, A.; Simon, P. Pharmacokinetics of PEGylated Gold Nanoparticles: In Vitro—In Vivo Correlation. *Nanomaterials* **2022**, *12*, 511.

(54) Rosa, S.; Connolly, C.; Schettino, G.; Butterworth, K. T.; Prise, K. M. Biological mechanisms of gold nanoparticle radiosensitization. *Cancer Nanotechnol.* **2017**, *8*, 2.

(55) Jaskólska, D. E.; Brougham, D. F.; Warring, S. L.; McQuillan, A. J.; Rooney, J. S.; Gordon, K. C.; Meledandri, C. J. *ACS Appl. Nano Mater.* **2019**, *2*, 2230−2240.

(56) Ahmad, R.; Schettino, G.; Royle, G.; Barry, M.; Pankhurst, Q. A.; Tillement, O.; Russell, B.; Ricketts, K. Radiobiological Implications of nanoparticles following radiation treatment. *Part. Part. Syst. Charact.* **2020**, *37*, No. 1900411.

(57) Yang, Y.; Zheng, X.; Chen, L.; Gong, X.; Yang, H.; Duan, X.; Zhu, Y. Multifunctional Gold Nanoparticles in Cancer Diagnosis and Treatment. *Int. J. Nanomed.* **2022**, *17*, 2041−2067.

(58) Singh, N.; Marets, C.; Boudon, J.; Millot, N.; Saviot, L.; Maurizi, L. In vivo protein corona on nanoparticles: does the control of all material parameters orient the biological behavior? *Nanoscale Adv.* **2021**, *3*, 1209−1229.

(59) Brix, N.; Samaga, D.; Belka, C.; Zitzelsberger, H.; Lauber, K. Analysis of clonogenic growth in vitro. *Nat. Protoc.* **2021**, *16*, 4963−4991.

(60) Subiel, A.; Ashmore, R.; Schettino, G. Standards and methodologies for characterizing radiobiological impact of high-Z nanoparticles. *Theranostics* **2016**, *6*, 1651−1671.

(61) Jain, S.; Coulter, J. A.; Hounsell, A. R.; Butterworth, K. T.; McMahon, S. J.; Hyland, W. B.; Muir, M. F.; Dickson, G. R.; Prise, K. M.; Currell, F. J.; et al. Cell-specific radiosensitization by gold nanoparticles at megavoltage radiation energies. *Int. J. Radiat. Onocol. Biol. Phys.* **2011**, *79*, 531−539.

(62) Seah, M. P.; Dench, W. A. Quantitative electron spectroscopy of surfaces: a standard data base for electron inelastic mean free paths in solids. *Surf. Interface Anal.* **1979**, *1*, 2−11.

(63) He, C.; Chow, J. C. L. Gold nanoparticle DNA damage in radiotherapy: A Monte Carlo study. *AIMS Bioeng.* **2016**, *3*, 352−361.

(64) Suzuki, Y.; Nishizawa, K.; Kurahashi, N.; Suzuki, T. Effective attenuation length of an electron in liquid water between 10 and 600 eV. *Phys. Rev. E. Stat. Nonlin. Soft Matter Phys.* **2014**, *90*, No. 010302.

(65) Shahhoseini, E.; Ramachandran, P.; Patterson, W. R.; Geso, M. Determination of dose enhancement caused by AuNPs with Xoft Axxent Electronic (eBx) and conventional brachytherapy: in vitro study. *Int. J. Nanomedicine* **2018**, *13*, 5733−5741.

(66) Aljohani, F. S.; Hamed, M. T.; Bakr, B. A.; Shahin, Y. H.; Abu-Serie, M. M.; Awaad, A. K.; El-Kady, H.; Elwakil, B. H. In vivo bio-distribution and acute toxicity evaluation of greenly synthesized ultra-

small gold nanoparticles with different biological activities. *Sci. Rep.* **2022**, *12*, 6269.